



One step flame-made fluorinated Pt/TiO₂ photocatalysts for hydrogen production



Gian Luca Chiarello^{a,b,*}, Maria Vittoria Dozzi^a, Marco Scavini^a, Jan-Dierk Grunwaldt^b, Elena Selli^a

^a Dipartimento di Chimica, Università degli Studi di Milano, via Golgi 19, 20133 Milano, Italy

^b Institute for Chemical Technology and Polymer Chemistry, Karlsruhe Institute of Technology, Engesserstrasse 20, 76131 Karlsruhe, Germany

ARTICLE INFO

Article history:

Received 21 February 2014

Received in revised form 29 April 2014

Accepted 3 May 2014

Available online 10 May 2014

Keywords:

Photocatalytic H₂ production

Methanol photo-steam reforming

Flame spray pyrolysis

Fluorinated TiO₂

In situ EXAFS

ABSTRACT

The photocatalytic production of hydrogen from methanol steam reforming was investigated over a series of fluorinated Pt/TiO₂ samples (F for O nominal molar substitution ranging from 5 to 15 at%) synthesized by flame spray pyrolysis in single step. The so obtained photocatalysts were characterized by BET, XRD, XPS, UV–vis absorption analyses and in situ X-ray absorption spectroscopy (XAS) at the Pt L3-edge. XPS analysis confirmed the presence of both surface and bulk fluorine. XAS revealed that Pt, mostly in oxidized form in the as prepared samples, readily reduced to the metallic form under gas-phase photocatalytic reaction conditions. Photocatalytic hydrogen production tests showed that 5 at% F for O substitution in TiO₂ led to an increase in the H₂ and CO₂ production rates, whereas above this value the H₂ production rate decreased linearly with increasing the nominal F loading in the photocatalyst. A significant increase of selectivity to CO₂, from 35% to 45%, was obtained over the best performing fluorinated photocatalyst with respect to the flame-made F-free one. Thus, TiO₂ fluorination favors the indirect methanol photo-oxidation mechanism by increasing surface hydroxyl radical formation with a consequent increase of selectivity toward CO₂ production. On the other hand, excessive fluorination introduces structural defects, acting as electron–hole recombination centers, and may hinder interface electron transfer, because of the F-induced surface electronegativity. Both effects concur to decrease photo-activity.

© 2014 Elsevier B.V. All rights reserved.

1. Introduction

Although a lot of new photocatalysts in different forms have been proposed in recent years and successfully tested in both thermodynamically up-hill (e.g. hydrogen production from water solutions) and down-hill reactions (photocatalytic oxidation of organic pollutants of water and air), titanium dioxide still remains the most employed and most investigated photocatalyst [1–3], mainly because of its outstanding photostability, together with its relatively good absorption and photoproduced charge separation properties. Different strategies have been employed to improve its performance as a photocatalyst [4], e.g. by enhancing its light absorption ability in the visible region through doping with non metal elements [5–7] or by achieving a better charge separation through surface modification by noble metals or different oxides

deposition [8,9]. Moreover, a wide variety of synthetic routes have been developed to prepare it in different forms and shapes, also with different surface area and porosity.

Fluorination, implying either surface modification (fluoride adsorption) or lattice-fluorine doping, is one of the strategies pursued to improve the photocatalytic performance of TiO₂. Surface fluorination consists in a simple ligand exchange reaction between fluoride anions and surface hydroxyl groups, which was found to induce drastic changes in both titanium dioxide surface properties and photoactivity, largely depending on the reaction substrate [10–15]. On the other hand, doping occurs when fluorine participates to the crystallization process of TiO₂ and leads to its modification in terms of phase, size, crystallinity, shape and exposed facets, also tuning the crystal organization into peculiar architectures and pore structures [16–21].

Both surface [22–25] and bulk [26–29] TiO₂ fluorination has been extensively investigated by some of us. Surface fluorination, achieved by exposing the semiconductor to aqueous solutions containing fluoride anions, was found to have positive effects on the hydroxyl radicals mediated photocatalytic degradation of organics in the aqueous phase, as unequivocally demonstrated by the

* Corresponding author at: Università degli Studi di Milano, Dipartimento di Chimica, via Golgi 19, I-20133 Milano, Italy. Tel.: +39 02 503 14281; fax: +39 02 503 14300.

E-mail address: gianluca.chiarello@unimi.it (G.L. Chiarello).

relatively large amounts of hydroxyl radicals detected on fluorinated titania by spin trapping EPR experiments [22]. Furthermore, fluoride anions adsorbed on the photocatalyst surface have a shielding effect on the photoproduced active species and favor their desorption and reaction in the liquid phase [23]. Surface fluorination also largely depends on the properties of the pristine TiO₂ material, remarkable photoactivity changes having been observed mainly in the case of P25 TiO₂ [25].

On the other hand, the increase in photoactivity induced by F-doping in TiO₂ materials prepared by sol–gel synthesis should be essentially related to the stabilization of the highly active anatase phase up to relatively high calcination temperature and to the consequent high crystallinity of the materials [26,27]. Moreover, intriguing synergistic effects of simultaneous bulk fluorine addition and surface modification by noble metal nanoparticles deposition have been recently evidenced in hydrogen production from water–methanol vapor mixtures with a series of NH₄F-doped TiO₂ photocatalysts [28].

Such reaction attracted much attention in recent years, because it provides a way to convert solar into chemical energy at room temperature and under atmospheric pressure, with a much lower CO₂ net production in comparison to the use of fossil fuels. Methanol is here employed as an organic electron donor able to scavenge the holes photoproduced in the semiconductor valence band much more efficiently than water itself. The reaction, which can be envisaged as a model reaction of photocatalytic H₂ production from renewable sources, has been investigated in previous studies by employing different TiO₂ based photocatalysts, containing different phases [30], or noble metal nanoparticles, prepared either by deposition of these latter on the TiO₂ surface, or by flame spray pyrolysis in one step, which were found to be best performing in this reaction [31,32].

Taking advantage of our previous experience in fluorine-modified materials and spray pyrolysis synthesis of metal-containing TiO₂ materials, in the present work we have explored the feasibility of producing, by flame spray pyrolysis in one step, fluorine-doped titania photocatalysts containing platinum nanoparticles. The materials obtained in this way were fully characterized by in situ X-ray analysis and tested in hydrogen production from methanol–water photocatalytic steam reforming.

2. Experimental

2.1. Photocatalysts preparation

Pt/TiO_{2-x}F_x ($x = 0, 0.10, 0.14, 0.20, 0.24$ and 0.30) were synthesized in continuous and single step by flame spray pyrolysis [33]. These samples were labeled as Pt/TiO₂ and Pt/TiO₂:F($z\%$) with z corresponding to the nominal F molar substitution for O, ranging from 5% to 15%. The nominal Pt loading was always 1.0 wt.%. The precursor organic solution was prepared by dissolving 0.03 mol of titanium(IV)-isopropoxide in a 10 vol.% propanoic acid in xylene solution (total volume 50 mL). Propanoic acid was used to dissolve the required amount of the platinum precursor (hexachloroplatinic acid hydrate). Hexafluorobenzene, added in different volumes in place of xylene, was employed as co-solvent and fluorine source.

The so obtained liquid organic solutions were fed to the burner at 4 mL min⁻¹ by a syringe pump through a capillary tube placed at the center of a vertical nozzle and dispersed by oxygen (5 L min⁻¹) at 3 bar constant pressure drop across the burner nozzle. The spray was ignited by a methane/oxygen flame ring surrounding the central nozzle, to form the main vertical flame. The produced powders were collected on a glass fiber filter (Whatman GF/A, 26 cm in diameter) placed on top of a cylindrical steel vessel surmounting the

flame reactor and connected to a vacuum pump (Busch Seco SV 1040C).

2.2. Photocatalysts characterization

The BET specific surface area (SSA) was measured by N₂ adsorption/desorption at 77 K on a BELSORP-mini, BEL (Japan) apparatus, after out-gassing in vacuo at 350 °C for at least 6 h. X-ray diffraction patterns were recorded with a Bruker D8 Advance diffractometer, using the Cu K α radiation ($\lambda = 1.54056 \text{ \AA}$), and compared with the Inorganic Crystal Structure Database (ICSD) data for phase identification. UV–vis diffuse reflectance was measured by a Perkin-Elmer Lambda 35 apparatus equipped with an integrating sphere (Lab-sphere RSA-PE-20).

X-ray photoelectron spectroscopy (XPS) measurements were performed using a Leybold LHS 10/12 apparatus equipped with a hemispherical electron energy analyzer using Al K α radiation (1486.6 eV). Photoelectron spectra were recorded in constant analyzer energy mode. The binding energies were referred to the C 1s peak at 284.6 eV.

2.2.1. In situ XRD measurements under annealing in He

In situ X-ray diffraction (XRD) measurements were collected at the PDIFF beamline of the ANKA synchrotron in Karlsruhe, Germany. The storage ring typically operated at 2.5 GeV electron energy and 180 mA injection current. The diffractograms were recorded by means of a “banana” 90° curved position sensitive detector, PSD Inel CPS590 (60 s counting time), using a monochromatic 16 keV ($\lambda = 0.7749 \text{ \AA}$) beam selected by a Si(1 1 1) double-crystal monochromator. The in situ experiments were carried out under He flux (20 mL min⁻¹) while heating at 10 °C min⁻¹ from 150 °C up to 800 °C, employing a quartz capillary reactor (inner diameter 0.8 mm) containing the as prepared photocatalyst sample, placed above a heating air blower.

The in situ recorded XRD patterns were analyzed using the Rietveld refinement method [34] as implemented in the GSAS software, with the EXPGUI graphical interface [35], by a strategy similar to that described in Ref. [36]. The background was fitted by Chebyshev polynomials. Adsorption correction was performed through the Lobanov empirical formula implemented for the Debye–Scherrer geometry. Line profiles were fitted using a modified pseudo-Voigt function.

In the last refinement cycles, scale factors, cell parameters and an average isotopic thermal parameter were allowed to vary, as well as background and line profile parameters. Because of the overlap of the Bragg peaks consequent to the co-presence of two titania polymorphs and of their nanocrystalline nature, no positional parameters were varied during the refinements.

2.2.2. In situ XAS at the Pt L3-edge

In situ X-ray absorption spectroscopy (XAS) studies at the Pt L3-edge (11,564 eV) were performed at the XAS beamline of the ANKA synchrotron, using a Si(1 1 1) double-crystal monochromator detuned to ca. 60% of the maximum intensity. Incident and transmitted X-ray intensity were measured by ion chambers (Oxford). Because of the low Pt loading the extended X-ray absorption fine structure (EXAFS) spectra were recorded in fluorescence mode using a five elements Low Energy Germanium detector (LEGe, Camberra-Eurisys). In particular, 50 mg of as prepared powder were loaded at the center of a quartz capillary (1.5 mm outer diameter; 0.02 mm wall thickness). The capillary was housed into a special home-made holder connected to the in- and out-let gas lines and placed at 45° with respect to the X-ray beam, facing the fluorescence detector [37,38]. The sample was left under a flowing 3.5% CH₃OH/3.8% H₂O/He balance gas mixture (20 mL min⁻¹) for 20 min in the dark followed by 2 h irradiation with an iron halogenide

Table 1
Specific surface area (SSA), crystal phase composition and mean crystallite size (from Rietveld refinement of XRD patterns) of the as prepared flame-made photocatalysts.

Sample	SSA (m ² g ⁻¹)	Phase composition (wt.%)		Mean crystallite size (nm)	
		Anatase	Rutile	Anatase	Rutile
TiO ₂	124	87	13	24	26
Pt/TiO ₂	119	85	15	21	24
Pt/TiO ₂ :F(5%)	134	89	11	20	15
Pt/TiO ₂ :F(7%)	130	91	9	16	23
Pt/TiO ₂ :F(10%)	142	89	11	15	19
Pt/TiO ₂ :F(12%)	135	87	13	16	21
Pt/TiO ₂ :F(15%)	132	86	14	22	26

mercury arc lamp (Jelosil, 250 W), placed above the quartz capillary and emitting in the 330–450 nm wavelength range. Quick EXAFS spectra at the Pt L₃-edge were measured every 3.5 min along the whole experiment (in the dark and under irradiation). Long EXAFS spectra at the Pt L₃-edge were measured before and after 2 h irradiation as well.

XAS data were analyzed using the IFEFFIT (Athena and Artemis) software [39]. Data fitting was performed in the R space on the Fourier-transformed k^3 -weighted EXAFS spectra (Fourier transform in the 2–12 Å⁻¹ k range). Theoretical scattering amplitudes and phase shifts of the Pt–Pt and Pt–O shells (first shell only) were calculated using the FEFF code [40].

2.3. Photocatalytic tests

The photocatalytic activity in hydrogen production from methanol photo-steam reforming was tested using the already described [31] closed stainless steel system. Briefly, the gas phase (3.5% CH₃OH/3.8% H₂O/N₂ balance), generated by bubbling the gas phase into a 20 vol.% CH₃OH in water solution, kept at 30 °C, was continuously recirculated at constant rate (40 mL min⁻¹) by means of a bellow pump through the photoreactor containing the photocatalyst powder (14 mg) deposited on 20–40 mesh (0.42–0.85 mm) sieved quartz grains. Prior to any run, the whole set-up was thoroughly flushed with inert gas in the dark, in order to remove any trace of oxygen. The recirculating gas phase composition was analyzed on-line with a gas chromatograph (GC, Agilent 6890N) equipped with two capillary columns (MolSieve 5A and HP-Plot Q), two detectors (Thermo Conductive, TCD, and Flame Ionization, FID) and a Ni catalyst for CO and CO₂ methanation. N₂ was employed as carrier gas. A 300 W Xe arc lamp (LOT-Oriel) was used as irradiation source, placed at 20 cm from the reactor, with a 11.7 mW cm⁻² irradiation intensity on the reactor in the 350 < λ < 400 nm range, as measured with an optical power meter (Thorlabs PM200) equipped with a thermal power sensor (Thorlabs S302C).

3. Results and discussion

3.1. Photocatalysts characterization

The flame-made materials are typically micro-aggregates of single crystal nanoparticles [31–33], thus possessing high SSA, often exceeding 100 m² g⁻¹. Indeed, one advantage of the flame method is the possibility to synthesize oxide powders at very high temperature (up to 2000 °C when xylene is used as solvent [41]) ensuring a good crystallinity, but with a short residence time within the flame (the central dispersion O₂ stream is usually at the speed of sound), thus preventing excessive crystal growth.

The results of the BET analysis and of the Rietveld refinement of the XRD patterns of the materials, reported in Table 1, show that the bare, flame-made TiO₂ sample consisted of a mixture of 87 wt.% anatase and 13 wt.% rutile with a SSA of 124 m² g⁻¹. The addition of Pt during the synthesis did not significantly affect the

titanium structure in terms of crystal phase composition and SSA. On the other hand, the fluorinated samples contained a slightly higher amount of anatase (up to ca. 91 wt.%) and a greater SSA, up to 142 m² g⁻¹ (Table 1). This increased SSA is also reflected by the smaller mean crystallite size of the anatase phase of the fluorinated samples, as calculated from Rietveld refinement of the XRD patterns [42]. No reflection of Pt could be observed in the XRD patterns because of the low particles size and Pt loading.

According to the UV–vis diffuse reflectance spectra (see Fig. S1, Supporting information), fluorinated flame-made TiO₂ exhibits an absorption threshold below 400 nm. The addition of Pt leads to an increase of the absorption baseline in the visible region (the sample color turns from white to grayish), but neither fluorine nor platinum addition affects the band gap absorption threshold. This is consistent with previous reports [16,26,43] and with theoretical calculations [6,44,45], evidencing that doping TiO₂ with F introduces localized high-density energy levels, composed of F 2p states, residing below the valence band of TiO₂.

3.2. XPS analysis

Titanium, oxygen and carbon, together with fluorine in fluorinated samples, are the only elements detected by XPS analysis on the surface of the flame-made materials. The XPS analysis in the Ti 2p region (Fig. 1) shows two peaks, due to spin–orbit coupling, located at a binding energy (BE) of ca. 459 eV (Ti 2p_{3/2}) and 465 eV (Ti 2p_{1/2}) typical of Ti⁴⁺ in TiO₂. No particular differences can be observed in the Ti 2p XPS spectra of the fluorinated samples, in line with the previous studies on fluorine-doped TiO₂ [27,46].

In contrast, significant differences appear in the O 1s region, as shown in Fig. 2, where two peaks appear at BE ca. 530 eV and 532 eV, attributed to oxygen atoms in the TiO₂ lattice and to surface OH groups, respectively [47]. The latter peak is predominant in the XPS pattern of TiO₂:F(5%) and its relative intensity with respect to the former decreases with increasing the nominal F for O substitution. This result is opposite to usual reports on XPS analysis of TiO₂. In fact, the O 1s core peak located at 532 eV usually appears as a low intensity shoulder of the predominant peak at 530 eV [48–50]. Recent studies on flame-made 50 at% F–TiO₂, presumably containing a higher amount of fluorine than the presently investigated materials [46], also evidenced a XPS O 1s pattern similar to that of Pt/TiO₂:F(15%) shown in Fig. 2. Thus, XPS analysis in the O 1s region reveals an exceptionally high hydroxyl surface coverage in our flame-made materials containing relatively low fluorine amounts, TiO₂:F(5%) in particular.

Finally, all of the as prepared fluorinated samples display a peak at 684.6 eV in the F 1s BE region (Fig. 3), attributed to surface chemisorbed fluoride [16,51]. However, this peak disappeared after etching with Ar and was replaced by a new signal at higher binding energy (686.5 eV). A similar behavior was observed with sol-gel synthesized F–TiO₂ [27] and also recently reported by Le et al. [48] for F-doped TiO₂ prepared by spray pyrolysis, the peak at 686.5 eV being ascribed in both cases to bulk fluorine atoms in the TiO₂

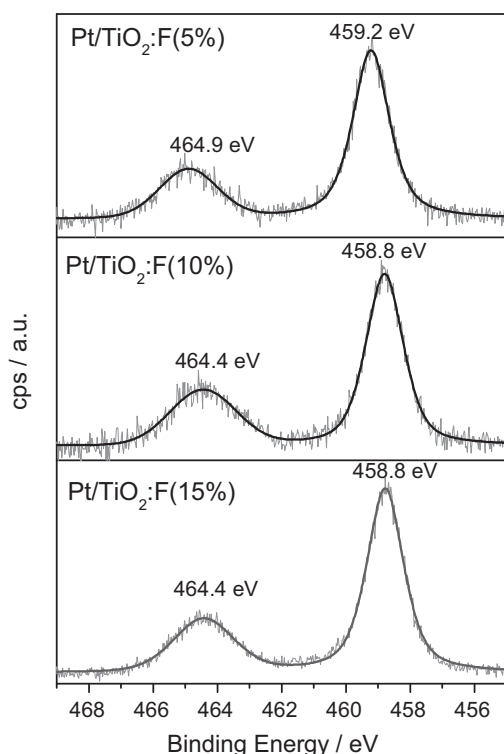


Fig. 1. XPS spectra of flame-made Pt/TiO₂:F(5%), Pt/TiO₂:F(10%) and Pt/TiO₂:F(15%) in the Ti 2p binding energy region.

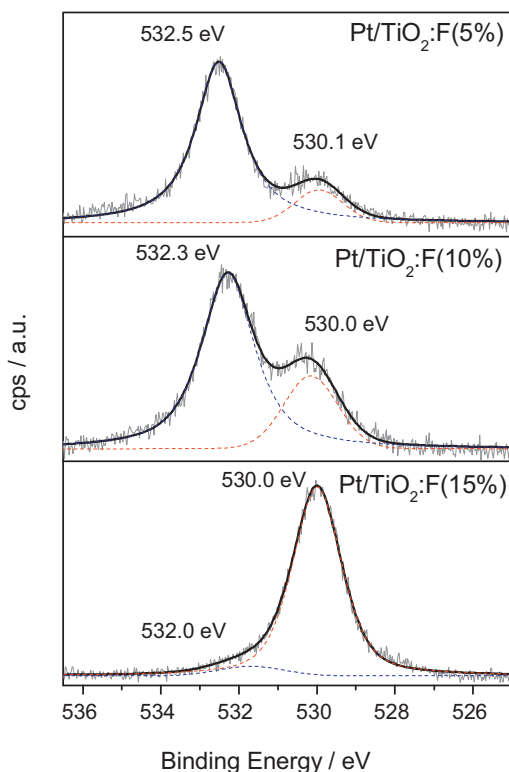


Fig. 2. XPS spectra of flame-made Pt/TiO₂:F(5%), Pt/TiO₂:F(10%) and Pt/TiO₂:F(15%) in the O 1s binding energy region.

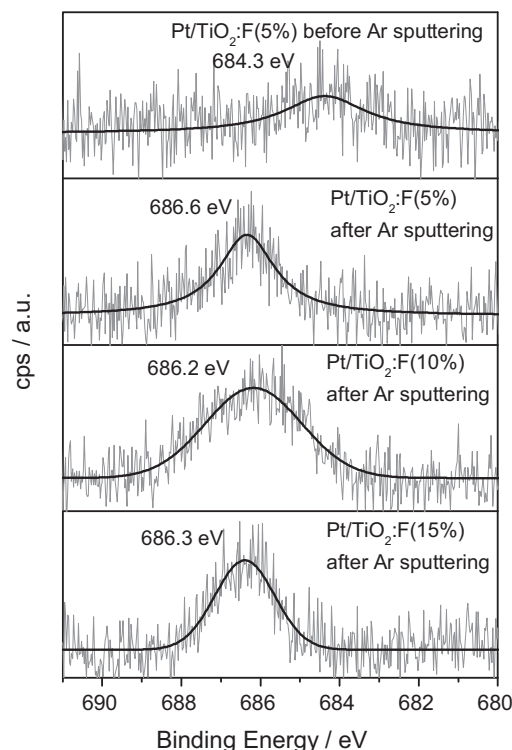


Fig. 3. XPS spectra (F 1s binding energy range) of as prepared flame-made Pt/TiO₂:F(5%) and of Pt/TiO₂:F(5%), Pt/TiO₂:F(10%) and Pt/TiO₂:F(15%) after etching with Ar.

lattice. It has been reported that bulk F can generate a XPS signal at BE from 685.3 eV (generally attributed to F in TiOF₂) [18,51] up to 688.5 eV [16,18,48,51], depending on the chemical environment. Hence, XPS analysis confirms the presence of both surface and bulk fluorine in our one step flame-made F–Pt/TiO₂ samples.

3.3. In-situ XRD analysis

Titania exists in three main crystal structures anatase (tetragonal), brookite (orthorhombic) and rutile (tetragonal), depending on how the TiO₆ octahedra are connected each other [30,52]. Lower packing density (3.9 g cm^{−3}) anatase structure usually exhibits higher photoactivity than rutile (4.3 g cm^{−3}), despite rutile has a slightly narrow band gap (ca. 3.0 eV) with respect to anatase (ca. 3.2 eV).

F-doped titania is usually prepared by wet chemistry methods in the presence of fluorine precursors, which favor the selective formation of highly crystalline anatase. The so obtained anatase phase is remarkably stable against phase transition [7,16,27], even up to 1100 °C [53], and this exceptional thermal stability is generally attributed to the high crystallinity of fluorinated titania prepared by wet chemistry methods. Indeed, the presence of bulk oxygen vacancies leads to discontinuity in the crystal lattice, favoring the rearrangement of TiO₆ octahedra into the more stable rutile phase.

The thermal stability of flame-made materials was tested by in situ XRD analysis upon annealing in flowing He up to 800 °C. The results obtained with the Pt/TiO₂ and Pt/TiO₂:F(10%) samples as a function of temperature are shown in Fig. 4 (see also Figs. S2 and S3). For both samples the main reflection of rutile at 2θ = 13.4° (corresponding to the 2θ = 27° reflection of the [1 1 0] plane detected under Cu Kα radiation) starts to increase at ca. 600 °C, due to anatase into rutile phase transition. However, above this temperature the intensity of the main reflection of anatase at 2θ = 12.35° (corresponding to the 2θ = 25° reflection of the [1 0 1] plane detected

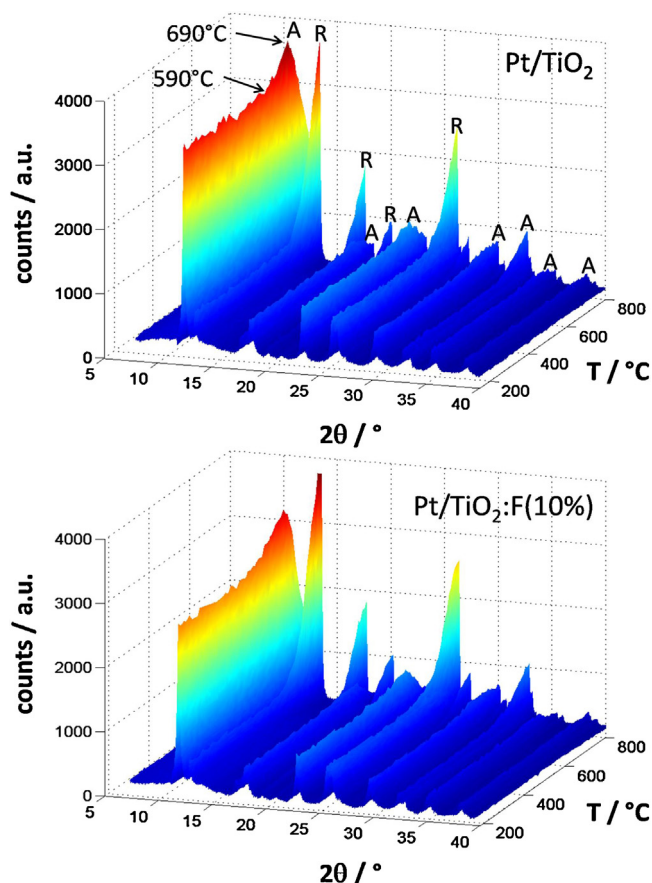


Fig. 4. In situ XRD patterns of flame made Pt/TiO₂ and Pt/TiO₂:F(10%) during annealing in flowing He from 150 °C up to 800 °C, with a 10 °C min^{−1} heating rate.

under Cu K α radiation) starts to increase as well, reaching a maximum at 690 °C, due to particles sintering, followed by a steep decrease. The evolution of the intensity of these two peaks with temperature suggests that the anatase into rutile phase transition proceeds in two steps, i.e. anatase nanoparticle sintering up to 690 °C, followed by anatase into rutile transformation.

Quantitative phase analysis obtained by Rietveld refinement of the in situ XRD patterns (Fig. S3) yielded the rutile weight fraction as a function of temperature in the two samples. As shown in Fig. 5, the anatase into rutile transition in the F-doped sample unexpectedly occurred at slightly lower temperature with respect to undoped Pt/TiO₂, up to a rutile content higher than in undoped Pt/TiO₂ after annealing at 800 °C (85 wt.% vs. 74 wt.%). Thus, in the case of the one step flame-made materials, anatase F-doped Pt/TiO₂ seems to own a lower thermal stability than undoped Pt/TiO₂, whereas the opposite was obtained for TiO₂ materials prepared by wet chemistry methods [27]. In that case, in fact, doping with fluorine, but also with other elements, usually stabilizes the anatase phase up to higher calcination temperature. The here observed effect of fluorine doping on anatase phase stability can be related to the lower particle size and to the greater number of crystal defects in flame-made materials. Furthermore, the present XRD investigation was performed under pure He stream, not in air. Annealing at high temperature under such conditions may cause bulk oxygen desorption which can increase the formation of oxygen vacancies after particle sintering. This effect is expected to be favored by the presence of F-doping.

Interesting results were obtained also by comparing the crystal unit cell volume of undoped and F-doped flame-made Pt/TiO₂, also determined by Rietveld refinement of the in situ XRD patterns.

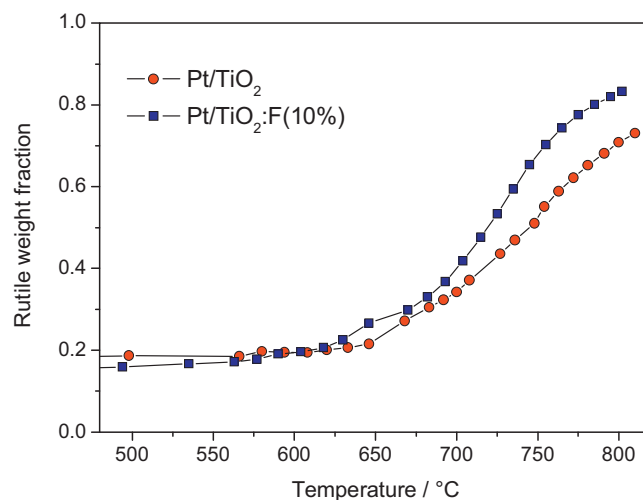


Fig. 5. Variation of the rutile weight fraction in flame-made Pt/TiO₂ (red circles) and Pt/TiO₂:F(10%) (blue squares) as a function of temperature during annealing in flowing He, obtained from Rietveld refinement of the in situ XRD patterns shown in Fig. 4. (For interpretation of the references to color in this figure legend, the reader is referred to the web version of this article.)

As shown in Fig. 6, the unit cell volume of both anatase and rutile phases increased linearly with temperature in both doped and undoped TiO₂, due to thermal expansion. The crystal unit cells of both anatase and rutile phases in the F-doped samples were almost constantly lower than those of the undoped material, over the whole investigated temperature range. This result can be accounted by the greater electronegativity of F compared with O, with a consequent slight shrinking of the Ti–F bond length. Indeed, the Ti–O bond length ranges from 1.9336 Å in anatase (ICSD file Nr 9852, tetragonal crystal system, space group *I41/amd*) to 1.9881 Å in rutile (ICSD file Nr 16636, tetragonal crystal system, space group *P42/mnm*), whereas the Ti–O and Ti–F bond length in TiOF₂ is 1.8990 Å (ICSD file Nr 38132, cubic crystal system, space group *Pm-3m*).

3.4. In-situ XAS analysis

The X-ray absorption spectra of the undoped and F-doped Pt/TiO₂ display an intense white line above the Pt L₃-edge at

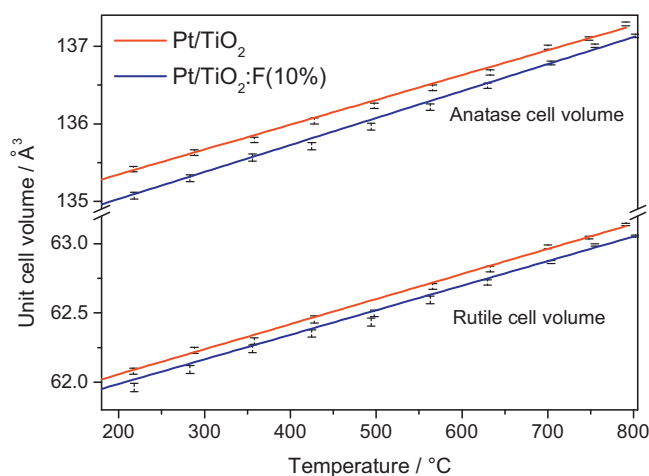


Fig. 6. Variation of the anatase and rutile crystal unit cell volume of flame-made Pt/TiO₂ (red line) and Pt/TiO₂:F(10%) (blue line) as a function of temperature during annealing in flowing He, obtained from Rietveld refinement of the in situ XRD patterns shown in Fig. 4. (For interpretation of the references to color in this figure legend, the reader is referred to the web version of this article.)

Table 2
Linear combination analysis results of XANES spectra at the Pt L3-edge.

Sample	PtO ₂ (mol%)	Pt (mol%)
Pt/TiO ₂	90	10
Pt/TiO ₂ :F(10%)	68	32
Pt/TiO ₂ :F(10%) after irradiation	33	67

an energy of 11,564 eV. Linear combination analysis of the X-ray absorption near edge structure (XANES) spectra (Fig. S4) with those of a reference Pt foil and of bulk α -PtO₂ (Table 2) indicates that only 10 mol% (undoped sample) and 32 mol% (F-doped sample) of Pt is present in reduced form in the as prepared photocatalysts. The k^3 -weighted Fourier transformed EXAFS spectra (Fig. S5) are dominated by a peak located at 1.63 Å followed by a minor peak at 2.85 Å (not corrected for phase shift), which can be ascribed to the Pt–O first coordination shell and to the Pt–(O)–Pt second coordination shell (partially overlapping with multiple scattering paths) in PtO₂, respectively. In contrast, the contribution at 2.5 Å due to the Pt–Pt first coordination shell in metallic Pt can hardly be detected. Thus, EXAFS analysis reveals that Pt is mostly present as PtO₂ in the as prepared samples.

Furthermore, in situ XANES spectra recorded under 3.5% CH₃OH/3.8% H₂O/He gas mixture flowing show no change of the Pt oxidation state in the absence of irradiation (Fig. 7), whereas Pt reduction clearly occurred under UV–vis irradiation at room temperature on both undoped and F-doped TiO₂ samples (see Figs. 7 and 8). Moreover, Fourier transformed EXAFS spectra (Fig. 9) show that a peak at 2.5 Å, due to the Pt–Pt first coordination shell in metallic Pt, appeared under UV–vis irradiation. Hence, in situ XAS investigation demonstrates that PtO₂ supported on TiO₂ is reduced to metallic Pt under photo-steam reforming reaction conditions, due to photopromoted electron transfer from the conduction band of the titania semiconductor to noble metal nanoparticles.

Pt reduction took place within the first irradiation hour, reaching a value around 67% of the overall Pt amount (Table 2 and Fig. 8), i.e. apparently Pt did not undergo complete reduction under irradiation. This is most probably due to the fact that UV–vis irradiation induces modification of only surface Pt nanoparticles, whereas X-rays penetrate the whole photocatalyst bed. Thus, XANES spectra may contain the contribution of PtO₂ present on a portion of the photocatalyst bed which cannot be reached by UV–vis light.

On the other hand, a closer look to the Fourier transformed EXAFS spectra (Fig. 9) reveals that the residual peak of the Pt–O shell is slightly shifted toward lower atomic distance. This shift is

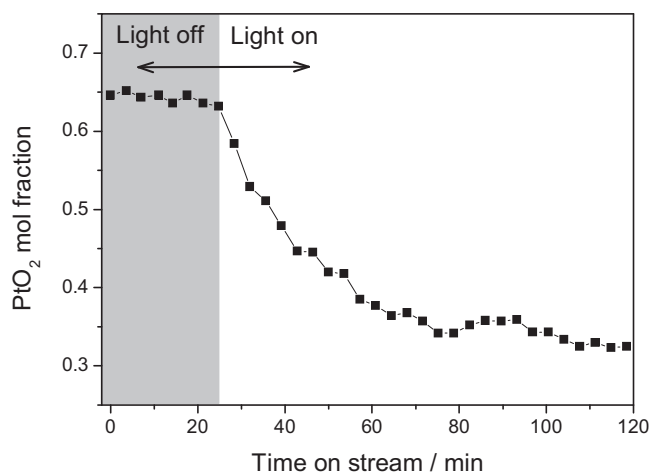


Fig. 7. PtO₂ molar fraction obtained by linear combination analysis of in situ XANES spectra at the Pt L3 edge of Pt/TiO₂:F(10%) under flowing 3.5% CH₃OH/3.8% H₂O/He gas mixture, kept in the dark for 20 min followed by UV–vis irradiation for 2 h.

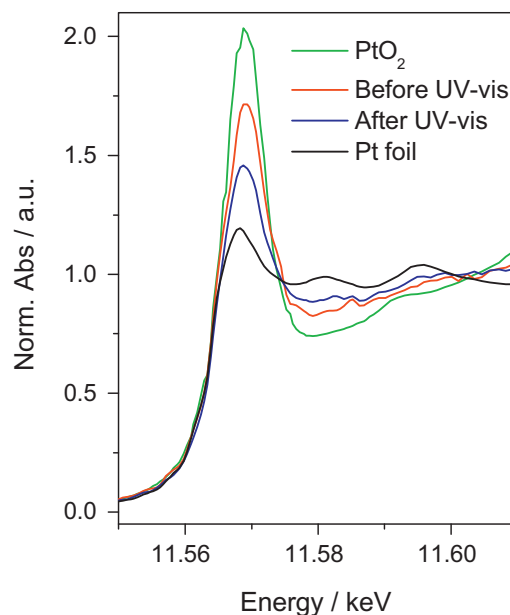


Fig. 8. In situ XANES spectra at the Pt L3-edge of Pt/TiO₂:F(10%) as prepared (red line) and after 2 h irradiation under flowing a 3.5% CH₃OH/3.8% H₂O/He gas mixture (blue line), in comparison with those of reference α -PtO₂ (green line) and Pt foil (black line). (For interpretation of the references to color in this figure legend, the reader is referred to the web version of this article.)

confirmed by the results of the spectral fitting reported in Table 3. In fact, the Pt–O interatomic distance shifts from 1.997 Å in the as prepared sample, very close to the 2.009 Å value of the PtO₂ reference, to 1.945 Å after irradiation. Furthermore, the Pt–O path degeneracy

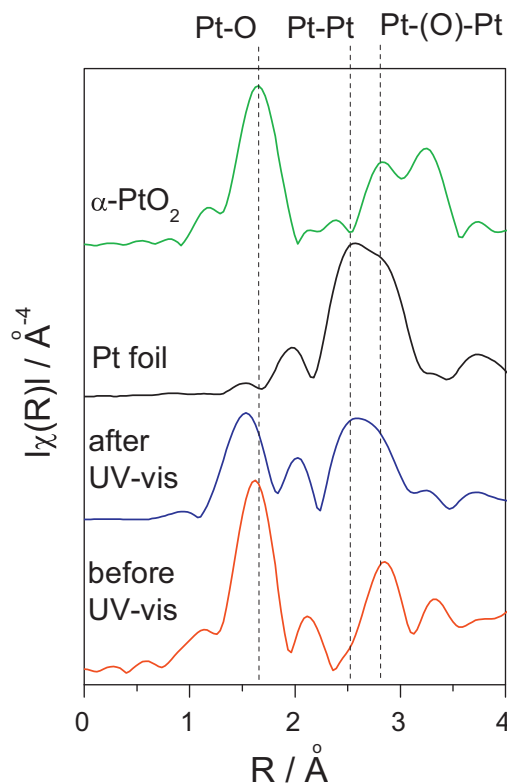


Fig. 9. In situ k^3 -weighted Fourier transformed EXAFS spectra at the Pt L3-edge (Fourier transformation in the 2–12 k range) of Pt/TiO₂:F(10%) as prepared and after 2 h irradiation under flowing 3.5% CH₃OH/3.8% H₂O/He gas mixture (blue line), in comparison with those of reference α -PtO₂ and Pt foil. The spectra are not phase corrected. (For interpretation of the references to color in this figure legend, the reader is referred to the web version of this article.)

Table 3
Fitting results of the EXAFS spectra at Pt L3-edge. S_0^2 = amplitude reduction factor; CN = coordination number; R = interatomic distance; σ^2 = Debye Waller factor (mean square disorder); ΔE_0 = energy shift.

Sample	Shell	S_0^2	CN	R (Å)	σ^2 (Å ²)	ΔE_0 (eV)
Pt foil	Pt–Pt	0.74 ± 0.03	12*	2.766 ± 0.001	0.0039 ± 0.0002	8.7 ± 0.2
Ref. PtO ₂	Pt–O	0.79 ± 0.2	6*	2.009 ± 0.012	0.0024 ± 0.0019	10.5 ± 2.1
Pt/TiO ₂ :F(10%) before irradiation	Pt–O	0.74*	5.0 ± 1.3	1.997 ± 0.018	0.0046 ± 0.0025	12.8 ± 3.2
Pt/TiO ₂ :F(10%) after irradiation	Pt–O	0.74*	2.5 ± 1.4	1.949 ± 0.024	0.0034 ± 0.006	6.8 ± 5.5
	Pt–Pt	0.79*	4.6 ± 0.9	2.769 ± 0.021	0.0033 ± 0.0008	

* Set parameters.

(i.e. the average coordination number) decreases after irradiation from 5.0 ± 1.3 (very close to 6 of bulk PtO₂) to 2.5 ± 1.4 , as well. Hence, the residual Pt–O shell, and consequently the incomplete Pt reduction occurring under UV–vis irradiation, may tentatively be attributed to the formation of a bridging Pt–O–Ti layer at the noble metal–semiconductor interface.

Finally, from the average coordination number of the Pt–Pt shell formed after UV–vis irradiation (4.6 vs. 12 for a bulk Pt foil, see Table 3) a mean size of metallic Pt nanoparticles can be estimated as ca. 10 Å [54], which is typical of single step flame-made materials [55].

3.5. Photocatalytic activity

The photocatalytic activity results in hydrogen production by photo-steam reforming of methanol over the investigated flame made materials are summarized in Fig. 10. According to the reaction mechanism proposed for this reaction [55,56], methanol is oxidized up to CO₂ through the formation of formaldehyde and formic acid as intermediate species. Traces of carbon monoxide, methane, methyl formate, acetaldehyde and dimethyl ether have been detected as main side products. The experimental set up operates under steady state condition, because the gas phase continuously recirculates and bubbles into the methanol in water liquid solution. Thus, the concentration of water and methanol vapors remains constant during the experiment as well as those of the intermediate species, i.e. formaldehyde and formic acid, being soluble (and accumulating) in the methanol aqueous solution. On the contrary, gaseous products, i.e. H₂, CO₂, CO and CH₄, accumulate in the recirculating gas phase and their concentration linearly increases within the time on stream (pseudo zero order kinetics). Their production rates can

thus be obtained as the slope of the straight concentration vs. time on stream plots.

As shown in Fig. 10, a 5% nominal F substitution for O led to an increase of the H₂ and CO₂ production rates. With photocatalysts containing more fluorine the rate of H₂ production decreased linearly with increasing the nominal F content. With F for O nominal substitution above 10% the rate of hydrogen production became even lower than that obtained with undoped Pt/TiO₂.

It is worth underlining that the hydrogen production rate obtained with the here investigated flame-made photocatalysts is higher than that recently obtained, under identical reaction conditions, with sol–gel prepared fluorine-doped materials containing 0.5 wt.% photodeposited Pt nanoparticles [28]. In that case a hydrogen production rate of $10.5 \text{ mmol h}^{-1} \text{ g}_{\text{cat}}^{-1}$ was attained with the best performing photocatalyst, i.e. 5% NH₄F-doped Pt/TiO₂, clearly lower than the H₂ production rate values reported in Fig. 10 for all flame-made Pt-containing TiO₂ materials. Interestingly, however, almost identical bell-shaped photoactivity trends were obtained also in that study [28] for naked, Au- and Pt-modified titania series with increasing the dopant content, demonstrating that the electronic structure of doped materials is crucial in determining photoproduced charge separation and mobility within the doped oxide photocatalysts. Present results indicate that both undoped and F-doped TiO₂ materials containing Pt nanoparticles prepared by flame spray pyrolysis in one step exhibit superior photocatalytic properties with respect to sol–gel prepared ones, at least in hydrogen production by photo-steam reforming of methanol, and also confirm the superiority of flame made Pt/TiO₂ with respect to benchmark P25 modified by Pt nanoparticles deposition [31,32].

Fig. 10 also shows that a significant increase of selectivity to CO₂, from 35% to 45%, was obtained with the best performing fluorinated photocatalyst, i.e. Pt/TiO₂:F(5%) in comparison to the F-free one. The selectivity to CO₂ strongly depends on the methanol to water molar ratio [55,56]. The present investigation has been performed employing an optimal CH₃OH/water molar ratio. Previous systematic studies carried out on this reaction as a function of the methanol molar fraction in the entire 0–1 range demonstrated that two different reaction paths are involved in methanol oxidation during the photo-steam reforming reaction: (i) a direct, valence band hole mediated path, and (ii) an indirect hydroxyl radical mediated path, which is more selective toward CO₂ production [55,56]. Hence, present results suggest that TiO₂ fluorination favors the indirect mechanism by increasing surface hydroxyl radical formation [10,11,22,23], consequently pushing the reaction toward higher CO₂ formation, with a consequent increase of hydrogen production rate. Indeed, according to the stoichiometry of the reaction, three moles of H₂ are produced per mole of methanol fully oxidized up to CO₂, whereas only two moles and one mole of H₂ are produced when it is oxidized only up to formic acid or formaldehyde, respectively.

On the other hand, excessive fluorination introduces detrimental effects both on the surface and in the bulk of TiO₂, leading to a reaction rate decrease, i.e., (i) a decrease of surface hydroxyl moieties (as shown by XPS analysis in Fig. 2), possibly leading also to lower methanol adsorption; and (ii) an obvious increase of bulk

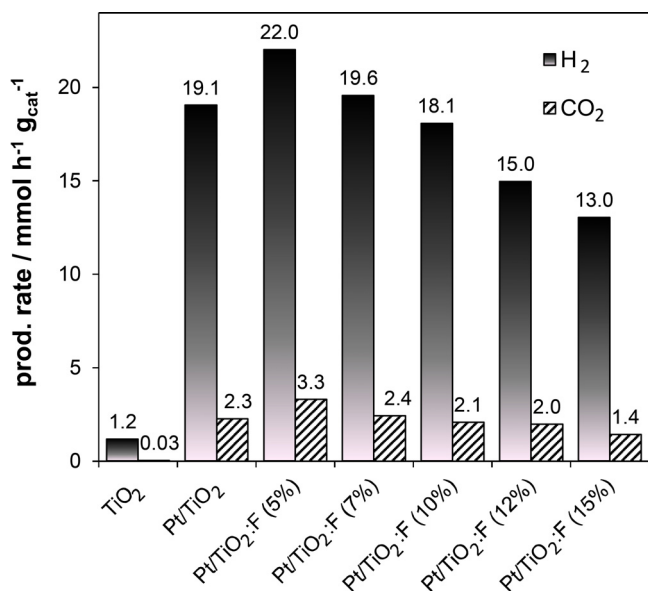


Fig. 10. Effect of fluorine nominal loading on the rates of H₂ and CO₂ photocatalytic production over one step flame-made fluorinated Pt/TiO₂.

structural defects, namely the formation of Ti^{3+} or Ti-vacancies, due to charge compensation effects of F for O substitution, which act as electron–hole recombination centers. Moreover, the transfer of CB electrons to electron acceptor species adsorbed on the photocatalyst surface or to the noble metal co-catalyst can be hindered because of the strong electronegativity of surface fluorine [11,23,57]. Such effect is expected to be more pronounced the higher is the F content, thus contributing to the decrease of photocatalytic performance of the materials observed at high F nominal content. Indeed, an increase in photocatalytic activity has been reported (e.g. [58]) after removing surface F by washing the photocatalyst with NaOH solutions. Thus, the photocatalytic performance of F-doped flame-made Pt/TiO₂ in hydrogen production is strongly affected by the nominal F content of the material, with beneficial effects on this reaction only at F for O nominal substitution below 10%.

4. Conclusions

Flame spray pyrolysis demonstrated to be an effective method for the continuous and single step synthesis of fluorinated, nanostructured Pt-containing titania photocatalysts. The introduction of monovalent fluoride during the synthesis, together with the short residence time of the growing oxide particles in the hottest zone of the flame, leads to the formation of nanocrystals undergoing an anatase into rutile phase transformation shifted to slightly lower temperature as well as a smaller anatase and rutile unit cell volume with respect to the F-free TiO₂ sample. Most interestingly, in situ XAS investigations at the Pt L3 edge revealed that Pt is mainly present in the oxidized PtO₂ form in the as prepared flame-made photocatalysts, but undergoes reduction to metallic Pt nanoparticles under photo-steam reforming reaction conditions.

A nominal F for O molar substitution lower than 10% leads to an unexpected increase of surface hydroxyl moieties which can favor the indirect hydroxyl mediated mechanism in the here investigated reaction, which is more selective toward complete methanol oxidation to CO₂, with the consequent increase of hydrogen production rate. On the other hand, fluorination exceeding 10% leads introduces an excess of bulk structural defects, acting as electron–hole recombination centers, and increases the F-induced surface electronegativity, inhibiting CB electron transfer. Both effects lead to a lower rate of photocatalytic hydrogen production.

Acknowledgments

The very active and skillful collaboration of Mike Mazzucchi in the experimental part of the work is fully acknowledged. ANKA is acknowledged for providing beam time, together with the BMBF-project “Materials in Action” for support to the catalysis infrastructure. In particular, the authors thank Stefan Mangold and Stephen Doyle for their support in XAS and XRD experiments, respectively. The collaboration of Francesca Riboni in XPS analysis is also gratefully acknowledged.

Appendix A. Supplementary data

Supplementary data associated with this article can be found, in the online version, at <http://dx.doi.org/10.1016/j.apcatb.2014.05.006>.

References

- [1] X. Chen, S.S. Mao, Chem. Rev. 107 (2007) 2891–2959.
- [2] A. Fujishima, X. Zhang, D.A. Tryk, Surf. Sci. Rep. 63 (2008) 515–582.
- [3] G. Liu, L. Wang, H.G. Yang, H.-M. Cheng, G.Q. Lu, J. Mater. Chem. 20 (2010) 831–843.
- [4] P.V. Kamat, J. Phys. Chem. C 116 (2012) 11849–11851.
- [5] S.G. Kumar, L.G. Devi, J. Phys. Chem. A 115 (2011) 13211–13241.
- [6] C. Di Valentini, G. Pacchioni, Catal. Today 206 (2013) 12–18.
- [7] M.V. Dozzi, E. Selli, J. Photochem. Photobiol., C: Photochem. Rev. 14 (2013) 13–28.
- [8] X. Hu, G. Li, J.C. Yu, Langmuir 26 (2010) 3031–3039.
- [9] Z. Wang, Y. Liu, B. Huang, Y. Dai, Z. Lou, G. Wang, X. Zhang, X. Qin, Phys. Chem. Chem. Phys. 16 (2014) 2758–2774.
- [10] C. Minero, G. Mariella, V. Maurino, E. Pelizzetti, Langmuir 16 (2000) 2632–2641.
- [11] H. Park, W. Choi, J. Phys. Chem. B 108 (2004) 4086–4093.
- [12] H. Kim, W. Choi, Appl. Catal., B: Environ. 69 (2007) 127–132.
- [13] J. Tang, H. Quan, J. Ye, Chem. Mater. 19 (2007) 116–122.
- [14] Q. Wang, C. Chen, D. Zhao, W. Ma, J. Zhao, Langmuir 24 (2008) 7338–7345.
- [15] D. Monllor-Satoca, T. Lana-Villarreal, R. Gómez, Langmuir 27 (2011) 15312–15321.
- [16] J.C. Yu, J.G. Ju, W. Ho, Z. Jiang, L. Zhang, Chem. Mater. 14 (2002) 3808–3816.
- [17] J.G. Yu, W.G. Wang, B. Cheng, B.L. Su, J. Phys. Chem. C 113 (2009) 6743–6750.
- [18] D. Li, H. Haneda, N.K. Labhsetwar, S. Hishita, N. Ohashi, Chem. Phys. Lett. 401 (2005) 579–584.
- [19] H.G. Yang, C.H. Sun, S.Z. Qiao, J. Zou, G. Liu, S.C. Smith, H.M. Cheng, C.Q. Lu, Nature 435 (2008) 638–641.
- [20] H.G. Yang, G. Liu, S.Z. Qiao, C.H. Sun, Y.G. Jin, S.C. Smith, J. Zou, H.M. Cheng, G.Q. Lu, J. Am. Chem. Soc. 131 (2009) 4078–4083.
- [21] M.V. Dozzi, E. Selli, Catalysts 3 (2013) 455–485.
- [22] M. Mrowetz, E. Selli, Phys. Chem. Chem. Phys. 7 (2005) 1100–1102.
- [23] M. Mrowetz, E. Selli, New J. Chem. 30 (2006) 108–114.
- [24] M.V. Dozzi, G.L. Chiarello, E. Selli, J. Adv. Oxid. Technol. 13 (2010) 305–312.
- [25] M.V. Dozzi, E. Selli, Catal. Today 206 (2013) 26–31.
- [26] M.V. Dozzi, S. Livraghi, E. Giamello, E. Selli, Photochem. Photobiol. Sci. 10 (2011) 343–349.
- [27] M.V. Dozzi, B. Ohtani, E. Selli, Phys. Chem. Chem. Phys. 13 (2011) 18217–18227.
- [28] M.V. Dozzi, A. Saccomanni, M. Altomare, E. Selli, Photochem. Photobiol. Sci. 12 (2013) 595–601.
- [29] M.V. Dozzi, C. D’Andrea, B. Ohtani, G. Valentini, E. Selli, J. Phys. Chem. C 117 (2013) 25586–25595.
- [30] G.L. Chiarello, A. Di Paola, L. Palmisano, E. Selli, Photochem. Photobiol. Sci. 10 (2011) 355–360.
- [31] G.L. Chiarello, L. Forni, E. Selli, Catal. Today 144 (2009) 69–74.
- [32] G.L. Chiarello, E. Selli, L. Forni, Appl. Catal., B: Environ. 84 (2008) 332–339.
- [33] G.L. Chiarello, I. Rossetti, L. Forni, J. Catal. 236 (2005) 251–261.
- [34] H.M. Rietveld, J. Appl. Cryst. 2 (1969) 65–71.
- [35] B.H. Toby, J. Appl. Cryst. 34 (2001) 210–213.
- [36] P. Ghigna, M. Scavini, C. Mazzoli, M. Brunelli, C. Laurenti, C. Ferrero, Phys. Rev. B: Condens. Matter 81 (2010) 073107.
- [37] J.-D. Grunwaldt, S. Hannemann, J. Göttlicher, S. Mangold, M. Denecke, A. Baiker, Phys. Scr. T. 115 (2005) 769–772.
- [38] J.-D. Grunwaldt, N. van Vegten, A. Baiker, Chem. Commun. (2007) 4635–4637.
- [39] B. Ravel, M. Newville, J. Synchrotron Radiat. 12 (2005) 537–541.
- [40] S.I. Zabinsky, J.J. Rehr, A. Ankudinov, R.C. Albers, M.J. Eller, Phys. Rev. B: Condens. Matter 52 (1995) 2995–3009.
- [41] G.L. Chiarello, I. Rossetti, P. Lopinto, G. Migliavacca, F. Forni, Catal. Today 117 (2006) 549–553.
- [42] D. Balzar, N. Audebrand, M.R. Daymond, A. Fitch, A. Hewat, J.L. Langford, A. Le Bail, D. Louër, O. Masson, C.N. McCowan, N.C. Popa, P.W. Stephens, B.H. Toby, J. Appl. Cryst. 37 (2004) 911–924.
- [43] A.M. Czoska, S. Livraghi, E. Giamello, S. Agnoli, G. Granozzi, E. Finazzi, C.D. Valentini, G. Pacchioni, J. Phys. Chem. C 112 (2008) 8951–8956.
- [44] T. Yamaki, T. Umehayashi, T. Sumita, S. Yamamoto, M. Maekawa, A. Kawasuso, H. Itoh, Nucl. Instrum. Methods Phys. Res., Sect. B 206 (2003) 254–258.
- [45] R. Asahi, T. Morikawa, T. Ohwaki, K. Aoki, Y. Taga, Science 293 (2001) 269–271.
- [46] Y. Jiang, J. Scott, R. Amal, Appl. Catal., B: Environ. 126 (2012) 290–297.
- [47] J.C. Dupin, D. Gonbeau, P. Vinatier, A. Levasseur, Phys. Chem. Chem. Phys. 2 (2000) 1319–1324.
- [48] T.K. Le, D. Flahaut, H. Martinez, T. Pigot, H.K.H. Nguyen, T.K.X. Huynh, Appl. Catal., B: Environ. 144 (2014) 1–11.
- [49] N. Kruse, S. Chenakin, Appl. Catal., A: Gen. 391 (2011) 367–376.
- [50] F. Riboni, L.G. Bettini, D.W. Bahnemann, E. Selli, Catal. Today 209 (2013) 28–34.
- [51] D. Li, H. Haneda, S. Hishita, N. Ohashi, Chem. Mater. 17 (2005) 2588–2595.
- [52] X. Bokhimi, A. Morales, M. Aguilar, J.A. Toledo-Antonio, F. Pedraza, Int. J. Hydrogen Energy 26 (2001) 1279–1287.
- [53] K. Lv, Q. Xiang, J. Yu, Appl. Catal., B: Environ. 104 (2011) 275–281.
- [54] A.I. Frenkel, C.W. Hills, R.G. Nuzzo, J. Phys. Chem. B 105 (2001) 12689–12703.
- [55] G.L. Chiarello, M.H. Aguirre, E. Selli, J. Catal. 273 (2010) 182–190.
- [56] G.L. Chiarello, D. Ferri, E. Selli, J. Catal. 280 (2011) 168–177.
- [57] D. Monllor-Satoca, R. Gomez, J. Phys. Chem. C 112 (2008) 139–147.
- [58] Z. Zheng, B. Huang, J. Lu, X. Qin, X. Zhang, Y. Dai, Chem. Eur. J. 17 (2011) 15032–15038.